

VistaDepth: Frequency Modulation With Bias Reweighting For Enhanced Long-Range Depth Estimation

Mingxia Zhan, Li Zhang*, XiaoMeng Chu and Beibei Wang*

Abstract—Monocular depth estimation (MDE) aims to predict per-pixel depth values from a single RGB image. Recent advancements have positioned diffusion models as effective MDE tools by framing the challenge as a conditional image generation task. Despite their progress, these methods often struggle with accurately reconstructing distant depths, due largely to the imbalanced distribution of depth values and an over-reliance on spatial-domain features. To overcome these limitations, we introduce VistaDepth, a novel framework that integrates adaptive frequency-domain feature enhancements with an adaptive weight-balancing mechanism into the diffusion process. Central to our approach is the Latent Frequency Modulation (LFM) module, which dynamically refines spectral responses in the latent feature space, thereby improving the preservation of structural details and reducing noisy artifacts. Furthermore, we implement an adaptive weighting strategy that modulates the diffusion loss in real-time, enhancing the model’s sensitivity towards distant depth reconstruction. These innovations collectively result in superior depth perception performance across both distance and detail. Experimental evaluations confirm that VistaDepth achieves state-of-the-art performance among diffusion-based MDE techniques, particularly excelling in the accurate reconstruction of distant regions.

Index Terms—Monocular Depth Estimation, Latent Frequency Modulation, Bias Reweighting, Latent Diffusion Models.

I. INTRODUCTION

Monocular depth estimation (MDE) is a fundamental task in computer vision, aiming to infer depth values from a single RGB image [1]. Accurate long-distance depth estimation is especially critical for applications such as virtual reality [4], autonomous driving [3], and robotics [2], where perceiving far-range geometry is essential for navigation planning, obstacle avoidance, and safe human-robot interaction.

Despite significant advancements, existing MDE methods often encounter considerable challenges concerning the precise reconstruction of distant depths. These difficulties are exacerbated by the long-tail distribution of depth values within training datasets, where near-region pixels are disproportionately more prevalent than those representing far regions. To further investigate this issue, our analysis across multiple depth datasets from various domains consistently highlights this skewed distribution toward near regions, as illustrated

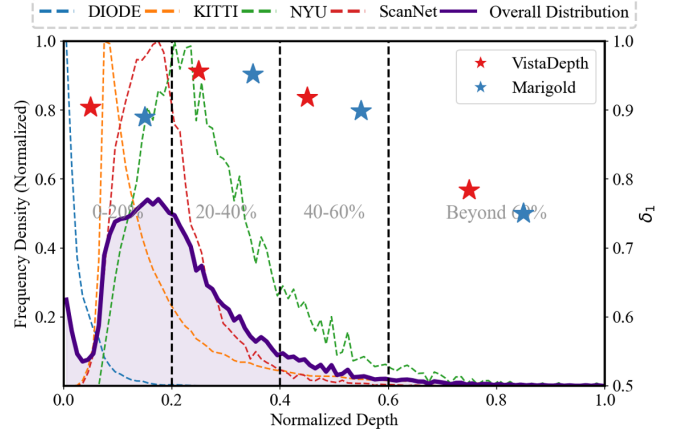


Fig. 1. An illustration of the long-tail depth distribution problem across multiple datasets, including DIODE, KITTI, NYUv2, and ScanNet. The purple curve represents the joint average distribution, highlighting the dominance of near-depth regions (0–20%) and the sparsity of far-depth regions (beyond 60%). The δ_1 is calculated as the average of the results on the NYUv2 and KITTI test datasets. VistaDepth (red star) consistently outperforms Marigold (blue star) across all depth intervals, particularly in distant regions.

in Fig. 1. This imbalance imposes substantial barriers to achieving accurate depth estimations at greater distances.

To address this issue, many discriminative learning methods have been developed with targeted strategies. These include distance-aware loss functions [34], which emphasize under-represented distant regions during training, and ensemble-based methods [35], which partition the depth range into intervals handled by specialized components. However, such discriminative models are typically trained on limited datasets and exhibit significant dependence on the underlying data distributions. Consequently, they often generalize poorly to unseen domains, which limits their applicability in real-world scenarios.

More recently, diffusion-based MDE approaches have demonstrated enhanced generalization capabilities across diverse domains, enabling zero-shot transfer to unseen datasets. Methods such as Marigold [27], GeoWizard [29], and DepthFM [28] leverage pre-trained Stable Diffusion backbones [25] to extract semantically rich latent representations. This enables high-quality depth predictions even when training with limited synthetic data. However, these models continue to encounter performance bottlenecks in far-depth regions due to two fundamental issues: (i) restricted modeling capacity resulting from purely spatial-domain representations, and (ii) the intrinsic long-tailed distribution of depth values in existing datasets.

In this paper, we propose VistaDepth, a diffusion-based

Mingxia Zhan is with the Hefei University of Technology, Hefei, Anhui, China (email: mxzhan@mail.hfut.edu.cn)

Li Zhang is with the Hefei University of Technology, Hefei, Anhui, China (email: lizhang@hfut.edu.cn)

Xiaomeng Chu is with the University of Science and Technology of China, Hefei, Anhui, China (email: cxmeng@mail.ustc.edu.cn)

Beibei Wang is with the Institute of Artificial Intelligence, Hefei Comprehensive National Science Center, Hefei, Anhui, China (email: wbb@iai.ustc.edu.cn)

Corresponding author: Li Zhang and Beibei Wang

MDE framework designed to explicitly address the two aforementioned limitations. First, we propose the Latent Frequency Modulation (LFM) module, which incorporates spectral information to enhance latent-space feature representations within the diffusion pipeline. The motivation behind LFM stems from the observation that distant regions in depth maps are typically characterized by low-frequency, smooth signals, which can become distorted or overshadowed by high-frequency artifacts introduced during the diffusion process. By adaptively balancing frequency contributions, LFM provides targeted frequency guidance directly in the latent space, enabling the diffusion process to better preserve geometric consistency and fine-grained structural details. Second, we present BiasMap, a depth-aware weighting mechanism. Our analysis across multiple benchmarks shows that applying a uniform loss over the entire depth range disproportionately emphasizes over-represented near-range samples, thereby degrading far-range accuracy. To mitigate this imbalance, BiasMap dynamically rebalances training emphasis based on both absolute distance and local depth transitions, generating adaptive weight maps that prioritize supervision toward distant and structurally complex regions. Together, LFM and BiasMap empower VistaDepth to focus supervision on critical distant regions while faithfully reconstructing their structure. Experimental results on diverse challenging indoor and outdoor datasets demonstrate that VistaDepth achieves state-of-the-art performance among diffusion-based MDE methods.

In summary, the key contributions of our work are outlined as follows:

- We introduce LFM, a frequency-domain enhancement module that refines latent features, leading to better structural consistency and detail preservation.
- We identify the long-tailed distribution of depth values as a core challenge in MDE and propose BiasMap to adaptively balance training across depth ranges.
- We present VistaDepth, a diffusion-based framework that achieves state-of-the-art performance in zero-shot MDE, with strong improvements in far-depth accuracy and fine-grained detail.

II. RELATED WORK

A. Monocular Depth Estimation

MDE is a structured regression task that aims to predict dense depth values from a single RGB image. With the rise of deep learning, Eigen et al. [6] introduced a pioneering multi-scale network, which was later improved upon by methods such as [5], [8], [10] using CNN frameworks, leading to performance gains. Subsequent works [7], [11] framed MDE as a density regression problem and proposed improved architectures [9], [12] to further boost accuracy. More recently, vision transformer architectures [13], [14] have achieved strong performance by capturing long-range dependencies and global context more effectively. Additionally, several studies have framed MDE as a combined classification-regression task, using adaptive binning techniques to discretize the continuous depth range. For instance, AdaBins [18] and BinsFormer [19] dynamically generate depth intervals conditioned on image

content, facilitating more precise depth estimations. Despite these advancements, all of the above discriminative methods are limited to models trained on a single dataset with fixed internal information (indoor or outdoor). As a result, their real-world performance often suffers in cross-domain or zero-shot.

B. Zero-Shot Monocular Depth Estimation

To address the domain gap in conventional MDE, recent efforts have shifted toward zero-shot MDE [16], [22], [31]–[33], aiming to predict accurate depth in unseen domains without any dataset-specific training. Early approaches such as MegaDepth [20] and DiverseDepth [21] utilize large-scale and diverse photo collections to encourage better generalization to novel real-world data. Recognizing that single-image depth estimation is inherently scale-ambiguous, some approaches explicitly adopt affine-invariant depth representation, which can facilitate better performance in downstream tasks. Recent approaches, such as DepthAnything [23], [24], build on DPT [16] and MiDaS [15], training on a 62M dataset for better generalization. However, these data-driven discriminative methods require large training resources and often produce overly smooth predictions for fine details. Recently, fine-tuning pre-trained diffusion models [30] has become a trend. Methods like Marigold [27], DepthFM [28], and Geowizard [29] leverage the latent diffusion model [25] to train monocular depth estimators with strong generalization, though they still struggle with distant region accuracy.

C. Long-Tail Distribution in Depth Estimation

One of the fundamental challenges in MDE lies in the long-tail distribution of depth values commonly observed in real-world datasets. In datasets such as NYUv2 [42] and KITTI [41], near-region pixels dominate the distribution, while far-region pixels are significantly underrepresented. This imbalance leads to biased models that favor frequent near-depth predictions, often at the expense of accurate estimation in distant regions. To address this, prior works have proposed tailored strategies within discriminative frameworks. For example, Jiao et al. [34] introduced attention-aware loss functions to upweight distant regions during training. Additionally, DME [35] have introduced Multi-Expert models that partition the depth range into intervals, with specialized components handling each interval to address this issue. However, generalization to unseen conditions and datasets remains a critical challenge, particularly in diverse real-world applications. Designing a unified approach that dynamically adapts to both rare and frequent depth ranges without compromising near-region precision represents a key unresolved issue in the field.

III. METHODOLOGY

A. Problem Formulation

Given an input image $x \in \mathbb{R}^{3 \times H \times W}$, the objective is to estimate a corresponding depth map, $d \in \mathbb{R}^{1 \times H \times W}$. Unlike traditional pixel-space regression approaches, we frame this task as learning the conditional distribution $D(d|x)$, using a latent diffusion probabilistic model. Specifically, we leverage

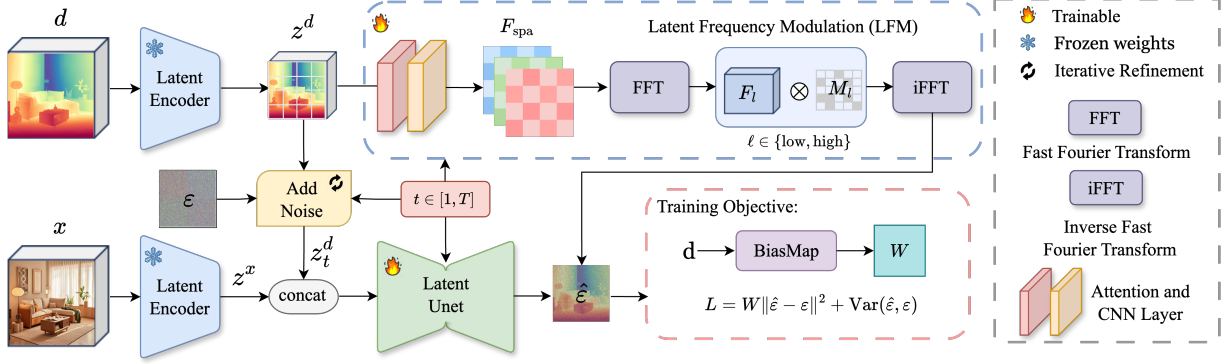


Fig. 2. **VistaDepth Training Pipeline.** The input RGB image x and depth d are encoded into the latent space via frozen VAE encoder. Noise is added to z_t^d at a uniformly sampled timestep $t \sim U(T)$. The concatenated (z^x, z_t^d) is fed into the U-Net, which predicts the added noise residual. Simultaneously, z_t^d is processed by the LFM module to generate a refined noise residual. The LFM module extracts z_t^d latent feature information, transforms it into the frequency space using FFT for detailed frequency decomposition, and finally returns the latent space using iFFT (see Section III-B for details). The training objective is to ensure that the final noise prediction $\hat{\epsilon}$ accurately corresponds to the noise added at timestep t .

a pretrained Variational Autoencoder (VAE) encoder $\mathcal{E}(\cdot)$ to transform both the RGB image and its corresponding depth map into a compact latent space:

$$z^x = \mathcal{E}(x), \quad z^d = \mathcal{E}(d),$$

where $z^x, z^d \in \mathbb{R}^{c \times h \times w}$ denote the latent representations for the RGB image and depth map, respectively.

In the forward diffusion process, noise is progressively added to the clean latent z_0^d over T discrete timesteps to produce a noisy latent z_t^d . Formally, the forward process is defined as:

$$z_t^d = \sqrt{\bar{\alpha}_t} z_0^d + \sqrt{1 - \bar{\alpha}_t} \epsilon_t, \quad \epsilon_t \sim \mathcal{N}(0, \mathbf{I}), \quad (1)$$

where $\bar{\alpha}_t = \prod_{s=1}^t (1 - \beta_s)$ is the cumulative product of variance schedule parameters β_s , and ϵ_t represents the added annealed multi-resolution noise (according to [46]). In this process, the U-Net network learns the noise added at timestep t , conditioned on the RGB latent z^x , while LFM module (detailed in Section III-B) simultaneously learns frequency-domain corrections to refine latent representations.

The reverse diffusion process iteratively removes noise using the U-Net and LFM. The reverse diffusion step is defined as:

$$z_{t-1}^d = z_t^d - [\epsilon_\theta(z_t^d, z^x, t) + \text{LFM}_t(z_t^d, t)], \quad (2)$$

where $\epsilon_\theta(z_t^d, z^x, t)$ denotes the noise predicted by the U-Net (which plays a leading role in the reverse process), and $\text{LFM}_t(\cdot)$ represents frequency-aware auxiliary refinements. After denoising, the refined latent z_0^d is decoded through the frozen VAE decoder $\mathcal{D}(\cdot)$ to reconstruct the final depth map.

B. Overview of VistaDepth Architecture

Our framework builds upon Stable Diffusion v2 [25], chosen for its computational efficiency and its ability to leverage robust image priors learned from large-scale data. VistaDepth is designed around leveraging the strengths of the latent diffusion model while explicitly addressing its inherent weaknesses. To counteract the long-tailed nature of depth data distribution and

further enhance distant-region performance, two key modules are introduced:

Latent Frequency Modulation (LFM). Diffusion-based MDE operates in a latent space where the model iteratively predicts added noise to reconstruct depth. However, in distant regions—characterized by flat textures and subtle gradients—the predicted noise often contains unstable high-frequency artifacts, leading to structural inconsistency and degraded reconstruction. These artifacts arise because distant regions exhibit weak image cues, making it harder for the diffusion model to infer coherent structures. Furthermore, the training data’s long-tail depth distribution underrepresents far-field samples, so the model lacks sufficient examples to denoise those latents accurately. As a result, frequency-domain distortions persist in distant areas where spatial-domain operations alone cannot compensate. To overcome this, we introduce the LFM module, a frequency-aware enhancement unit that operates in synergy with the U-Net during each denoising step. Given the noised latent z_t^d at diffusion timestep t , we first enrich its features by

$$F_{\text{spa}} = \text{Conv}_{3 \times 3}(\text{MHSA}(z_t^d)), \quad (3)$$

where Multi-head Self-attention captures global structure and a 3×3 convolution sharpens local details. We denote the output as F_{spa} . Next, we transform F_{spa} into the frequency domain using a 2D Fast Fourier Transform (FFT):

$$F_{\text{fft}} = \mathcal{F}(F_{\text{spa}}), \quad (4)$$

and split this complex tensor at a learnable cutoff R (initialized to half the maximum frequency radius and refined during training) into low- and high-frequency bands:

$$F_{\text{low}} = F_{\text{fft}} \odot \mathbf{1}(r \leq R), \quad F_{\text{high}} = F_{\text{fft}} \odot \mathbf{1}(r > R). \quad (5)$$

To enhance frequency-domain feature representations, the low- and high-frequency bands are each reshaped by concatenating their real and imaginary components into a $2C$ -channel feature map. Specifically, for each frequency band $\ell \in \{\text{low}, \text{high}\}$, we construct:

$$G_{\text{cat}} = \text{concat}(\text{Re}(F^\ell), \text{Im}(F^\ell)) \in \mathbb{R}^{2C \times H \times W}. \quad (6)$$

This reshaped feature map is then passed through a lightweight bottleneck network to predict a spatial gating mask $M_\ell \in [0,1]^{1 \times H \times W}$. The bottleneck consists of two sequential 1×1 convolutions, with the first convolution $W_1^{(\ell)}$ operating on G_{cat} , followed by a ReLU activation, and the second convolution $W_2^{(\ell)}$ generating the final mask. Specifically, the mask for each frequency band $\ell \in \{\text{low}, \text{high}\}$ is computed as follows:

$$M_\ell = \sigma \left(W_2^{(\ell)} * \text{ReLU} \left(W_1^{(\ell)} * G_{cat} \right) \right), \quad (7)$$

where $*$ denotes the 1×1 convolution operation, and σ is the sigmoid activation function. The output mask M_ℓ is then broadcast across channels to effectively suppress high-frequency noise while preserving important structural features. The two gated spectra are then combined as

$$F_{\text{mod}} = M_{\text{low}} \odot F_{\text{low}} + M_{\text{high}} \odot F_{\text{high}}, \quad (8)$$

and transformed back into the spatial domain using the inverse FFT:

$$F_{\text{fft}} = \mathcal{F}^{-1}(F_{\text{mod}}). \quad (9)$$

Finally, the output is fused with the original spatial features via residual addition:

$$F_{\text{global}} = F_{\text{spa}} + F_{\text{fft}}. \quad (10)$$

BiasMap Reweighting Mechanism. To address the supervision imbalance introduced by the long-tailed distribution of depth values, we propose BiasMap, a latent-space adaptive weighting mechanism designed to enhance model sensitivity to distant and structurally complex areas. Operating entirely within the latent representation space, BiasMap integrates seamlessly into the diffusion-based generative process. BiasMap dynamically emphasizes structurally meaningful depth regions during training, and is disabled at inference. It consists of two complementary components: an *Edge Weight Map* and a *Distance Weight Map*.

1) *Edge Weight Map*: The edge weight map is designed to focus the model’s attention on regions with significant depth discontinuities, which are critical for accurate depth boundary prediction. Specifically, we compute the edge map from the latent depth gradients using the Sobel operator as:

$$w_{\text{edge}} = \frac{\sqrt{G_x^2 + G_y^2}}{\max \left(\sqrt{G_x^2 + G_y^2} \right)}, \quad (11)$$

where G_x and G_y are the gradients in the horizontal and vertical directions, respectively. The resulting weights are normalized to the range $[0,1]$, ensuring stable application to the latent space. Critically, we observed empirically that uniformly emphasizing edges across all depth ranges tends to bias the training toward abundant near-field structures, causing the network to prematurely converge to suboptimal local minima. This observation aligns with prior findings in diffusion-based MDE frameworks, which inherently capture detailed textures [28]. Therefore, we apply it selectively to distant regions by computing a latent edge mask from depth gradients in pixel space and restricting it to areas beyond the 70th percentile of the depth range. This targeted emphasis

improves far-region structure without overly weighting trivial or texture-rich near regions.

2) *Distance Weight Map*: The distance weight map is designed to increase the model’s attention to distant regions by adaptively reweighting supervision based on pixel-space depth values. The key idea is to assign higher weights to pixels that are statistically deeper than the average in their own image. To achieve this, we compute a self-normalized weight using a sigmoid function:

$$w_{\text{distance}}(x, y) = \text{sig} \left(\frac{z_{\text{mean}}(x, y) - \mu}{\sigma + \epsilon} \right), \quad (12)$$

where $z_{\text{mean}}(x, y) = \frac{1}{C} \sum_{c=1}^C z_c(x, y)$ is the mean latent depth at (x, y) , $\text{sig}(\cdot)$ is the sigmoid activation, μ and σ are the per-image mean and standard deviation of z_{mean} , and ϵ is a small constant for numerical stability. To precisely localize supervision on structurally informative distant regions, we combine the two maps using element-wise multiplication:

$$w_{\text{combined}} = w_{\text{distance}} \cdot w_{\text{edge}}. \quad (13)$$

This design enforces an “AND-gate” behavior, assigning high weight only to pixels that are both statistically distant and exhibit strong depth discontinuities. Unlike weighted-sum fusion, which may overemphasize trivial distant regions (e.g., sky) or irrelevant nearby edges, the multiplicative form naturally suppresses such false positives. As a result, supervision is tightly concentrated on distant boundaries, leading to more robust optimization and improved far-field structure recovery.

Loss Function. At each sampled timestep t , the model predicts the noise $\hat{\epsilon}_t = \epsilon_\theta(z_t^d, z^x, t) + \text{LFM}_t(z_t^d, t)$, and the ground truth noise ϵ_t is derived from the forward process. The final loss function integrates the previously defined BiasMap. The loss is defined as:

$$\mathcal{L}_{\text{latent}} = \frac{1}{N} \sum_{i=1}^N w_{\text{combined}, i} \cdot \|\hat{\epsilon}_{t,i} - \epsilon_{t,i}\|^2, \quad (14)$$

where w_{combined} is the BiasMap, and N denotes the total number of latent elements. To prevent overfitting to high weight pixels, we introduce a variance regularization term:

$$\mathcal{L}_{\text{var}} = \frac{1}{N} \sum_{i=1}^N \text{Var}(\hat{\epsilon}_{t,i} - \epsilon_{t,i}), \quad (15)$$

which penalizes large variances across the latent space. This encourages the model to maintain stability across both low-weight and high-weight regions. The final objective is a weighted sum of the two terms:

$$\mathcal{L}_{\text{total}} = \mathcal{L}_{\text{latent}} + \mathcal{L}_{\text{var}}. \quad (16)$$

This two-part loss design forms a complete training loop that aligns well with the generative nature of diffusion models while addressing the supervision imbalance caused by depth distribution skew.

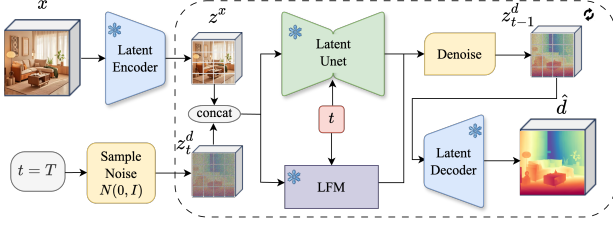


Fig. 3. **VistaDepth Inference Pipeline.** The input x is combined with Gaussian noise and passed through the denoising U-Net and LFM, which iteratively reduces noise in the latent space. Then decoded by the frozen VAE to produce the final depth map.

C. Training Strategy

The inference pipeline is illustrated in Fig. 2. Given an RGB image and its ground-truth depth, we first encode them into latent representations using a pretrained VAE. We sample a random timestep $t \in [1, T]$, and apply the forward diffusion process to obtain a noisy depth latent z_t^d . The backbone U-net and LFM then learn to denoise z_t^d by predicting the added noise ϵ_t , conditioned on the RGB latent z^x and timestep t .

D. Inference Strategy

The inference pipeline is illustrated in Fig. 3. During inference, BiasMap is entirely disabled, as it serves only to reweight supervision signals during training. The inference process relies solely on the U-Net denoiser and the LFM module. The process begins with the input RGB x concatenated with randomly generated noise. This noisy latent representation is progressively refined through an iterative denoising process. The U-Net predicts the added noise at each timestep, gradually reducing the noise level in the latent representation. Concurrently, the LFM module enhances the latent features by integrating frequency-domain information through selective masking and fusion. The final depth map is then reconstructed by decoding this refined latent representation using the frozen VAE decoder.

IV. EXPERIMENT

A. Implementation Details

We initialize our backbone network using the pre-trained weights from Stable Diffusion [25] and fine-tune only the U-Net. The latent diffusion backbone uses a pre-trained VAE with a downsampling factor of $r = 8$ and $c = 4$ channels. Meanwhile, LFM module operates in this latent space. During training, we employ the DDPM noise scheduler [47] with 1000 diffusion steps, while at inference, the DDIM scheduler [48] is used with 50 steps. The final predictions are obtained by averaging the results across 8 inference runs, each with different noise seeds. The model is trained for 14,000 steps using the AdamW optimizer, with a learning rate of 3×10^{-5} and a batch size of 8 by default. Our model takes approximately one day to train using single NVIDIA A100 GPU.

B. Benchmarking and Comparative Evaluation

Training datasets. We follow Marigold [27] and use 74K samples from two synthetic datasets, Hypersim [43] and Virtual KITTI [39]. Hypersim consists of 54K samples of indoor scenes with RGB images and depth maps resized to 480×640 . Virtual KITTI provides 20K samples of outdoor driving scenes across four scenarios with varied conditions.

Evaluation Datasets and Protocol. We evaluate our model on five real-world datasets that were not used in training: NYUv2 [42], an indoor dataset with 654 images; ScanNet [40], where we randomly sample 800 images from 312 validation scenes; KITTI [41], an outdoor driving dataset with sparse LiDAR depth, evaluated on the Eigen split with 652 images; ETH3D [44], evaluated on all 454 samples with ground truth; and DIODE [45], which covers both indoor and outdoor scenes, tested on 325 indoor and 446 outdoor images. The model’s performance is assessed using two metrics: Absolute Mean Relative Error (AbsRel), defined as $\frac{1}{N} \sum_{i=1}^N \left| \frac{d_i - \hat{d}_i}{d_i} \right|$ and δ_1 accuracy, which measures the percentage of pixels satisfying $\max \left(\frac{d_i}{\hat{d}_i}, \frac{\hat{d}_i}{d_i} \right) < 1.25$.

Comparisons with Other Models. As shown in Tab. I, our VistaDepth achieves consistently strong performance across six diverse benchmarks, outperforming all other diffusion-based methods and rivaling top discriminative models despite using significantly fewer training samples. Notably, VistaDepth ranks first among generative approaches on four out of six datasets and secures second-best results globally on NYUv2 [42], KITTI [41], ScanNet [40], and DIODE [45]. Fig. 4 further highlights the qualitative improvements, showcasing the model’s ability to accurately capture fine-grained details and predict depth in distant regions. Fig. 6 demonstrates VistaDepth’s zero-shot capability and its superior performance in recognizing distant regions, proving its robustness and effectiveness in-the-wild applications.

C. Ablation Studies

Depth Range Evaluation. To validate the VistaDepth against long-tailed distributions, we conducted ablation studies by segmenting the test datasets into four depth regions to evaluate performance across varying depths. As shown in Table II, compared to Marigold [27], our method not only maintains excellent performance in near regions but also significantly enhances accuracy in far regions.

Ablation on BiasMap. In this part, we excluded the LFM module to isolate the impact of BiasMap. As shown in Table III, adding the distance weight map or edge weight map alone improves performance. The optimal results are achieved by combining both the distance and edge weight maps, demonstrating their complementary roles in improving model robustness across varying distributions.

Ablation on Edge Weight Map Threshold. We study how the percentile threshold P , used to restrict the edge weight map to distant regions, affect performance on the KITTI and NYUv2 datasets. Preliminary results show a clear upward trend in accuracy as P increases from 0% to 60%, indicating that excluding near-field edges is beneficial. However, as

TABLE I

QUANTITATIVE COMPARISON WITH AFFINE-INVARIANT DEPTH ESTIMATORS ON ZERO-SHOT BENCHMARKS. METHODS ARE CATEGORIZED INTO *Discriminative* AND *Generative* TYPES. "#TRAIN" INDICATES THE NUMBER OF TRAINING SAMPLES. EVALUATION METRICS INCLUDE ABSREL (LOWER IS BETTER) AND δ_1 (HIGHER IS BETTER). **BOLD** VALUES DENOTE THE BEST WITHIN EACH METHOD TYPE, AND UNDERLINED VALUES DENOTE THE SECOND-BEST WITHIN EACH TYPE. GLOBAL BEST AND SECOND-BEST VALUES ACROSS ALL METHODS ARE HIGHLIGHTED WITH SUPERSCRIPTS \star AND \star , RESPECTIVELY.

Type	Method	#Train	NYUv2		KITTI		ETH3D		ScanNet		DIODE	
			AbsRel↓	δ_1 ↑	AbsRel↓	δ_1 ↑	AbsRel↓	δ_1 ↑	AbsRel↓	δ_1 ↑	AbsRel↓	δ_1 ↑
<i>Discriminative</i>	DiverseDepth [21]	320K	11.7	87.5	19.0	70.4	22.8	69.4	10.9	88.2	37.6	63.1
	MiDaS [15]	2M	11.1	88.5	23.6	63.0	18.4	75.2	12.1	84.6	33.2	71.5
	LeReS [36]	354K	9.0	91.6	14.9	78.4	17.1	77.7	9.1	91.7	27.1	<u>76.6</u>
	OmniData [22]	12.2M	7.4	94.5	14.9	83.5	16.6	77.8	<u>7.5</u>	93.6	33.9	74.2
	HDN [21]	300K	6.9	94.8	11.5	86.7	<u>12.1</u>	83.3	8.0	93.9	<u>24.6</u> \star	78.0
	DPT [16]	1.4M	9.8	90.3	<u>10.0</u>	<u>90.1</u>	7.8	94.6	8.2	93.4	18.2 \star	75.8
	Depth Anything [23]	63.5M	4.3 \star	98.1 \star	7.6 \star	94.7 \star	12.7	<u>88.2</u>	4.2 \star	98.0 \star	27.7	75.9
<i>Generative</i>	Marigold [27]	74K	5.5	96.4	<u>9.9</u>	<u>91.6</u>	6.5	96.0	6.4	95.1	30.8	77.3
	DepthFM [28]	63K	6.5	95.6	<u>10.1</u>	90.9	9.4	90.9	8.5	92.3	25.1	78.3 \star
	GeoWizard [29]	280K	<u>5.4</u>	<u>96.6</u>	10.3	89.2	<u>6.4</u> \star	<u>96.1</u> \star	<u>6.1</u>	<u>95.3</u>	30.6	77.6
	VistaDepth (Ours)	74K	<u>5.2</u> \star	<u>97.4</u> \star	<u>9.7</u> \star	<u>91.8</u> \star	6.3 \star	96.3 \star	<u>5.9</u> \star	<u>95.4</u> \star	<u>29.6</u>	<u>78.1</u> \star

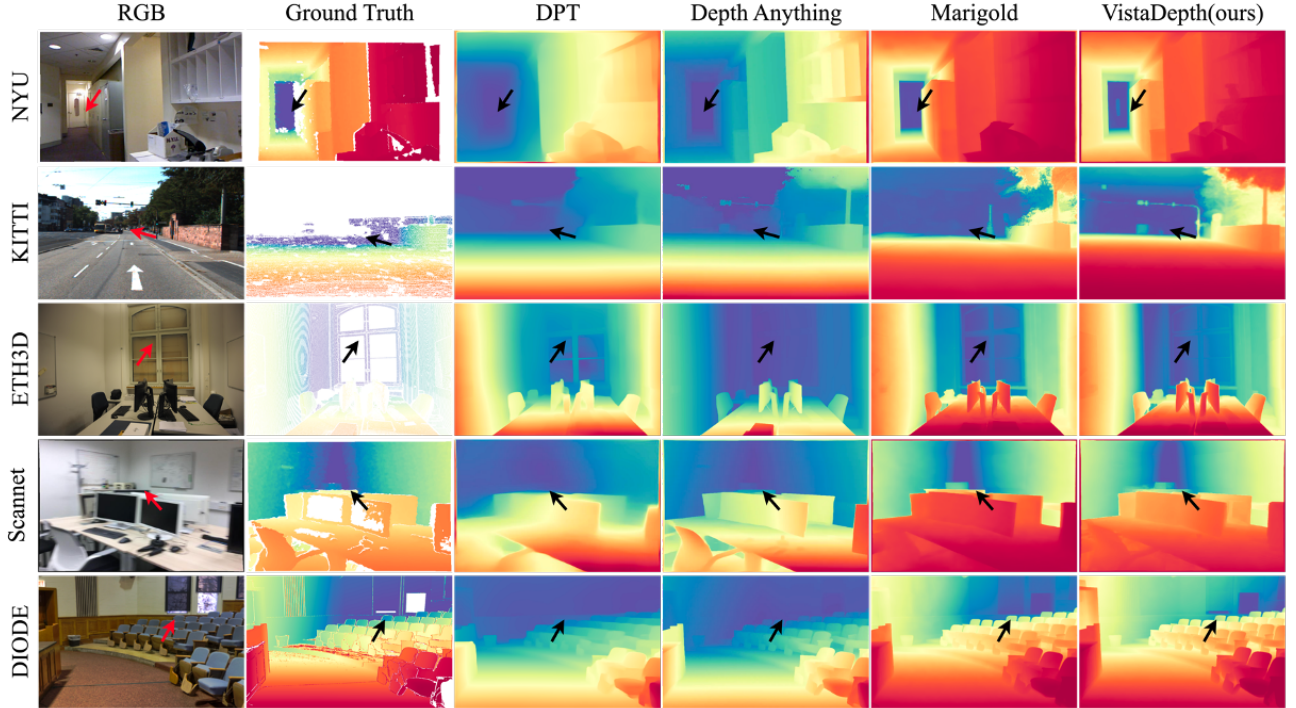


Fig. 4. Qualitative comparison of MDE across different datasets. VistaDepth demonstrates superior performance in capturing distance fine details (e.g., edges of doorways in NYU, distant cars in KITTI, windows in ETH3D and DIODE) and maintaining scene consistency (e.g., complex interior scene in ScanNet).

TABLE II

PERFORMANCE COMPARISON BETWEEN WEIGHTED AND UNWEIGHTED ACROSS INDOOR AND OUTDOOR DATASETS.

Depth Range	NYUv2 (Indoor)		KITTI (Outdoor)	
	ours	Marigold [27]	ours	Marigold [27]
0-20%	91.1	89.6	89.7	88.3
20-40%	97.9	97.5	93.4	92.9
40-60%	92.8	91.1	90.9	88.7
Beyond 60%	79.6	75.1	77.2	74.9

TABLE III

EVALUATES THE IMPACT OF THE DISTANCE WEIGHT MAP AND EDGE WEIGHT MAP ON MODEL PERFORMANCE.

Edge	Distance	NYUv2 (Indoor)		KITTI (Outdoor)	
		AbsRel ↓	δ_1 ↑	AbsRel ↓	δ_1 ↑
\times	\times	6.7	94.8	11.1	89.1
\times	\checkmark	5.7	95.9	10.7	90.6
\checkmark	\times	5.5	96.3	10.1	91.1
\checkmark	\checkmark	5.4	96.8	9.9	91.4

shown in Fig 5, setting too high removes informative mid-range structures and leads to degraded performance. We find that $P = 70\%$ offers the best balance, effectively suppressing

redundant details while enhancing supervision on structurally meaningful distant boundaries.

Ablation Study on LFM Components. We conduct

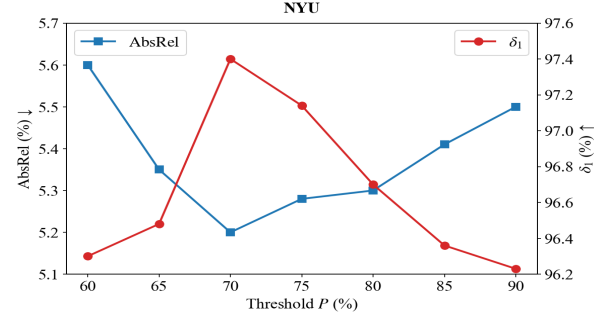
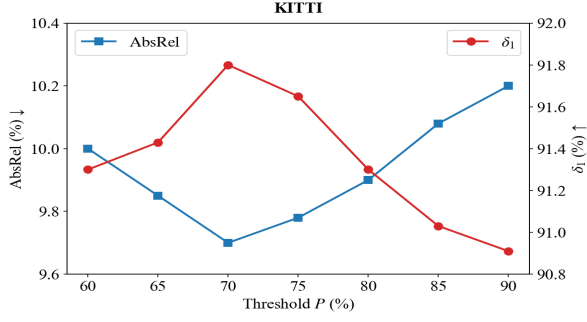


Fig. 5. Performance evaluation on the KITTI and NYUv2 datasets with varying thresholds P . The results show that the 70th percentile achieves the best trade-off between near-region accuracy (δ_1) and far-region prediction (AbsRel) on both datasets.

TABLE IV
ABLATION STUDY ON LFM COMPONENTS.

Models	NYUv2 (Indoor)		KITTI (Outdoor)	
	AbsRel ↓	δ_1 ↑	AbsRel ↓	δ_1 ↑
Baseline	6.7	94.8	11.1	89.1
+ SACM	6.2	95.2	10.7	90.3
+ SACM + Split	5.6	96.1	10.4	90.9
Full LFM	5.3	96.9	9.9	91.5

Quantitative results in Table IV validate the effectiveness of these modules across both NYUv2 [42] and KITTI [41] datasets.

V. CONCLUSION

In this paper, we present VistaDepth, a novel framework for monocular depth estimation that alleviates the challenges posed by the long-tail distribution of depth values. By integrating adaptive supervision via latent frequency modulation and BiasMap, VistaDepth improves depth prediction—particularly in distant regions that are often overlooked by existing models. Our improvements are especially crucial for safety-critical applications like autonomous driving, where early and accurate perception of distant obstacles is essential for timely decision-making. Experiments demonstrate that VistaDepth consistently outperforms existing diffusion-based monocular depth estimators and generalizes well across diverse real-world scenarios.

REFERENCES

- [1] V. Arampatzakis, G. Pavlidis, N. Mitianoudis, and N. Papamarkos, “Monocular depth estimation: A thorough review,” *IEEE Transactions on Pattern Analysis and Machine Intelligence*, vol. 46, no. 4, pp. 2396–2414, 2024.
- [2] X. Dong, M. A. Garratt, S. G. Anavatti, and H. A. Abbass, “Towards real-time monocular depth estimation for robotics: A survey,” *IEEE Transactions on Intelligent Transportation Systems*, vol. 23, no. 10, pp. 16 940–16 961, 2022.
- [3] G. Li, X. Chi, and X. Qu, “Depth estimation based on monocular camera sensors in autonomous vehicles: A self-supervised learning approach,” *Automotive Innovation*, vol. 6, no. 2, pp. 268–280, 2023.
- [4] A. Rasla and M. Beyeler, “The relative importance of depth cues and semantic edges for indoor mobility using simulated prosthetic vision in immersive virtual reality,” in *Proceedings of the 28th ACM Symposium on Virtual Reality Software and Technology*, ser. VRST ’22. New York, NY, USA: Association for Computing Machinery, 2022. [Online]. Available: <https://doi.org/10.1145/3562939.3565620>
- [5] W. Yuan, X. Gu, Z. Dai, S. Zhu, and P. Tan, “New crfs: Neural window fully-connected crfs for monocular depth estimation. arxiv 2022,” *arXiv preprint arXiv:2203.01502*, 2022.
- [6] D. Eigen, C. Puhrsch, and R. Fergus, “Depth map prediction from a single image using a multi-scale deep network,” *Advances in neural information processing systems*, vol. 27, 2014.
- [7] Z. Zhang, Z. Cui, C. Xu, Y. Yan, N. Sebe, and J. Yang, “Pattern-affinitive propagation across depth, surface normal and semantic segmentation,” in *Proceedings of the IEEE/CVF conference on computer vision and pattern recognition*, 2019, pp. 4106–4115.
- [8] H. Fu, M. Gong, C. Wang, K. Batmanghelich, and D. Tao, “Deep ordinal regression network for monocular depth estimation,” in *Proceedings of the IEEE conference on computer vision and pattern recognition*, 2018, pp. 2002–2011.

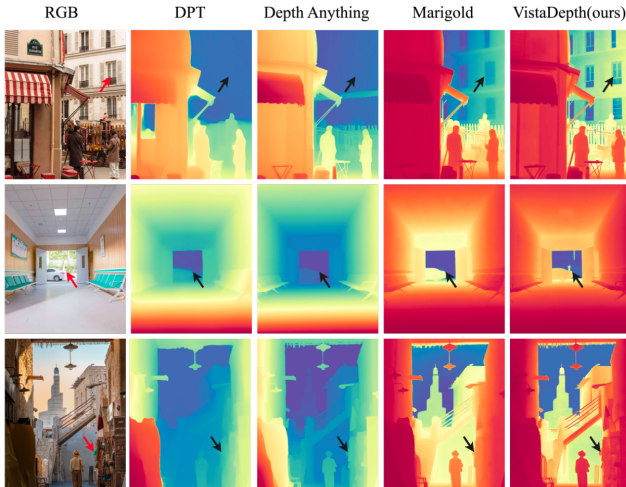


Fig. 6. **Qualitative comparisons on in-the-wild samples.** Red indicates the near plane and blue denotes the far plane. Discriminative models such as DPT [16] and Depth Anything [23] produce robust depth predictions but tend to oversmooth fine details. Diffusion-based methods like Marigold [27] better preserve local structures and textures. VistaDepth further enhances distant depth reconstruction and detail fidelity, demonstrating clear advantages in both depth range accuracy and geometric sharpness.

ablations to evaluate each component within LFM, excluding BiasMap to isolate its standalone effect. Starting from the baseline U-Net, we first introduce the Spatial Attention-Convolution Module (SACM), which substantially enhances spatial feature representations through combined local convolutions and global self-attention (row “+ SACM”). Incorporating the spectral Split further mitigates high-frequency artifacts by enabling independent low/high gating, yielding additional gains (row “+ SACM + Split”). Finally, the Bottleneck mask network refines this gating with minimal overhead, delivering the best overall performance (row “Full LFM”). Each successive addition yields measurable incremental improvements.

- [9] J. Yan, H. Zhao, P. Bu, and Y. Jin, "Channel-wise attention-based network for self-supervised monocular depth estimation," in *2021 International Conference on 3D vision (3DV)*. IEEE, 2021, pp. 464–473.
- [10] J. H. Lee, M.-K. Han, D. W. Ko, and I. H. Suh, "From big to small: Multi-scale local planar guidance for monocular depth estimation," *arXiv preprint arXiv:1907.10326*, 2019.
- [11] L. Huynh, P. Nguyen-Ha, J. Matas, E. Rahtu, and J. Heikkilä, "Guiding monocular depth estimation using depth-attention volume," in *Computer Vision—ECCV 2020: 16th European Conference, Glasgow, UK, August 23–28, 2020, Proceedings, Part XXVI 16*. Springer, 2020, pp. 581–597.
- [12] S. Aich, J. M. U. Vianney, M. A. Islam, and M. K. B. Liu, "Bidirectional attention network for monocular depth estimation," in *2021 IEEE International Conference on Robotics and Automation (ICRA)*. IEEE, 2021, pp. 11 746–11 752.
- [13] Z. Li, Z. Chen, X. Liu, and J. Jiang, "Depthformer: Exploiting long-range correlation and local information for accurate monocular depth estimation," *Machine Intelligence Research*, vol. 20, no. 6, pp. 837–854, 2023.
- [14] G. Yang, H. Tang, M. Ding, N. Sebe, and E. Ricci, "Transformer-based attention networks for continuous pixel-wise prediction," in *Proceedings of the IEEE/CVF International Conference on Computer vision*, 2021, pp. 16 269–16 279.
- [15] R. Ranftl, K. Lasinger, D. Hafner, K. Schindler, and V. Koltun, "Towards robust monocular depth estimation: Mixing datasets for zero-shot cross-dataset transfer," *IEEE transactions on pattern analysis and machine intelligence*, vol. 44, no. 3, pp. 1623–1637, 2020.
- [16] R. Ranftl, A. Bochkovskiy, and V. Koltun, "Vision transformers for dense prediction," in *Proceedings of the IEEE/CVF international conference on computer vision*, 2021, pp. 12 179–12 188.
- [17] S. F. Bhat, R. Birkel, D. Wofk, P. Wonka, and M. Müller, "Zoedepth: Zero-shot transfer by combining relative and metric depth," *arXiv preprint arXiv:2302.12288*, 2023.
- [18] S. F. Bhat, I. Alhashim, and P. Wonka, "Adabins: Depth estimation using adaptive bins," in *Proceedings of the IEEE/CVF conference on computer vision and pattern recognition*, 2021, pp. 4009–4018.
- [19] Z. Li, X. Wang, X. Liu, and J. Jiang, "Binsformer: Revisiting adaptive bins for monocular depth estimation," *IEEE Transactions on Image Processing*, 2024.
- [20] Z. Li and N. Snavely, "Megadepth: Learning single-view depth prediction from internet photos," in *Proceedings of the IEEE conference on computer vision and pattern recognition*, 2018, pp. 2041–2050.
- [21] W. Yin, X. Wang, C. Shen, Y. Liu, Z. Tian, S. Xu, C. Sun, and D. Renyin, "Diversedepth: Affine-invariant depth prediction using diverse data," *arXiv preprint arXiv:2002.00569*, 2020.
- [22] A. Eftekhar, A. Sax, J. Malik, and A. Zamir, "Omnidata: A scalable pipeline for making multi-task mid-level vision datasets from 3d scans," in *Proceedings of the IEEE/CVF International Conference on Computer Vision*, 2021, pp. 10 786–10 796.
- [23] L. Yang, B. Kang, Z. Huang, X. Xu, J. Feng, and H. Zhao, "Depth anything: Unleashing the power of large-scale unlabeled data," in *Proceedings of the IEEE/CVF Conference on Computer Vision and Pattern Recognition*, 2024, pp. 10 371–10 381.
- [24] L. Yang, B. Kang, Z. Huang, Z. Zhao, X. Xu, J. Feng, and H. Zhao, "Depth anything v2," *arXiv preprint arXiv:2406.09414*, 2024.
- [25] R. Rombach, A. Blattmann, D. Lorenz, P. Esser, and B. Ommer, "High-resolution image synthesis with latent diffusion models," in *Proceedings of the IEEE/CVF conference on computer vision and pattern recognition*, 2022, pp. 10 684–10 695.
- [26] C. Schuhmann, R. Beaumont, R. Vencu, C. Gordon, R. Wightman, M. Cherti, T. Coombes, A. Katta, C. Mullis, M. Wortsman *et al.*, "Laion-5b: An open large-scale dataset for training next generation image-text models," *Advances in Neural Information Processing Systems*, vol. 35, pp. 25 278–25 294, 2022.
- [27] B. Ke, A. Obukhov, S. Huang, N. Metzger, R. C. Daudt, and K. Schindler, "Repurposing diffusion-based image generators for monocular depth estimation," in *Proceedings of the IEEE/CVF Conference on Computer Vision and Pattern Recognition*, 2024, pp. 9492–9502.
- [28] M. Gui, J. S. Fischer, U. Prestel, P. Ma, D. Kotovenko, O. Grebenkova, S. A. Baumann, V. T. Hu, and B. Ommer, "Depthfm: Fast monocular depth estimation with flow matching," *arXiv preprint arXiv:2403.13788*, 2024.
- [29] X. Fu, W. Yin, M. Hu, K. Wang, Y. Ma, P. Tan, S. Shen, D. Lin, and X. Long, "Geowizard: Unleashing the diffusion priors for 3d geometry estimation from a single image," in *European Conference on Computer Vision*. Springer, 2025, pp. 241–258.
- [30] S. Saxena, C. Herrmann, J. Hur, A. Kar, M. Norouzi, D. Sun, and D. J. Fleet, "The surprising effectiveness of diffusion models for optical flow and monocular depth estimation," *Advances in Neural Information Processing Systems*, vol. 36, 2024.
- [31] V. Guizilini, I. Vasiljevic, D. Chen, R. Ambrus, and A. Gaidon, "Towards zero-shot scale-aware monocular depth estimation," in *Proceedings of the IEEE/CVF International Conference on Computer Vision*, 2023, pp. 9233–9243.
- [32] W. Yin, C. Zhang, H. Chen, Z. Cai, G. Yu, K. Wang, X. Chen, and C. Shen, "Metric3d: Towards zero-shot metric 3d prediction from a single image," in *Proceedings of the IEEE/CVF International Conference on Computer Vision*, 2023, pp. 9043–9053.
- [33] S. Saxena, J. Hur, C. Herrmann, D. Sun, and D. J. Fleet, "Zero-shot metric depth with a field-of-view conditioned diffusion model," *arXiv preprint arXiv:2312.13252*, 2023.
- [34] J. Jiao, Y. Cao, Y. Song, and R. Lau, "Look deeper into depth: Monocular depth estimation with semantic booster and attention-driven loss," in *Proceedings of the European conference on computer vision (ECCV)*, 2018, pp. 53–69.
- [35] S. Yu, Y. Wang, Y. Zhuge, L. Wang, and H. Lu, "Dme: Unveiling the bias for better generalized monocular depth estimation," in *Proceedings of the AAAI Conference on Artificial Intelligence*, vol. 38, no. 7, 2024, pp. 6817–6825.
- [36] W. Yin, J. Zhang, O. Wang, S. Niklaus, L. Mai, S. Chen, and C. Shen, "Learning to recover 3d scene shape from a single image," in *Proceedings of the IEEE/CVF Conference on Computer Vision and Pattern Recognition*, 2021, pp. 204–213.
- [37] C. Zhang, W. Yin, B. Wang, G. Yu, B. Fu, and C. Shen, "Hierarchical normalization for robust monocular depth estimation," *Advances in Neural Information Processing Systems*, vol. 35, pp. 14 128–14 139, 2022.
- [38] Y. Zhong, B. Li, L. Tang, S. Kuang, S. Wu, and S. Ding, "Detecting camouflaged object in frequency domain," in *Proceedings of the IEEE/CVF conference on computer vision and pattern recognition*, 2022, pp. 4504–4513.
- [39] Y. Cabon, N. Murray, and M. Humenberger, "Virtual kitti 2," *arXiv preprint arXiv:2001.10773*, 2020.
- [40] A. Dai, A. X. Chang, M. Savva, M. Halber, T. Funkhouser, and M. Nießner, "ScanNet: Richly-annotated 3d reconstructions of indoor scenes," in *Proceedings of the IEEE conference on computer vision and pattern recognition*, 2017, pp. 5828–5839.
- [41] A. Geiger, P. Lenz, and R. Urtasun, "Are we ready for autonomous driving? the kitti vision benchmark suite," in *2012 IEEE conference on computer vision and pattern recognition*. IEEE, 2012, pp. 3354–3361.
- [42] N. Silberman, D. Hoiem, P. Kohli, and R. Fergus, "Indoor segmentation and support inference from rgb-d images," in *Computer Vision—ECCV 2012: 12th European Conference on Computer Vision, Florence, Italy, October 7–13, 2012, Proceedings, Part V 12*. Springer, 2012, pp. 746–760.
- [43] M. Roberts, J. Ramapuram, A. Ranjan, A. Kumar, M. A. Bautista, N. Paczan, R. Webb, and J. M. Susskind, "Hypersim: A photorealistic synthetic dataset for holistic indoor scene understanding," in *Proceedings of the IEEE/CVF international conference on computer vision*, 2021, pp. 10 912–10 922.
- [44] T. Schops, J. L. Schonberger, S. Galliani, T. Sattler, K. Schindler, M. Pollefeys, and A. Geiger, "A multi-view stereo benchmark with high-resolution images and multi-camera videos," in *Proceedings of the IEEE conference on computer vision and pattern recognition*, 2017, pp. 3260–3269.
- [45] I. Vasiljevic, N. Kolkin, S. Zhang, R. Luo, H. Wang, F. Z. Dai, A. F. Daniele, M. Mostajabi, S. Basart, M. R. Walter *et al.*, "Diode: A dense indoor and outdoor depth dataset," *arXiv preprint arXiv:1908.00463*, 2019.
- [46] G. Xu, Y. Ge, M. Liu, C. Fan, K. Xie, Z. Zhao, H. Chen, and C. Shen, "Diffusion models trained with large data are transferable visual models," *arXiv preprint arXiv:2403.06090*, 2024.
- [47] T. Salimans and J. Ho, "Progressive distillation for fast sampling of diffusion models," *arXiv preprint arXiv:2202.00512*, 2022.
- [48] J. Song, C. Meng, and S. Ermon, "Denoising diffusion implicit models," *arXiv preprint arXiv:2010.02502*, 2020.
- [49] J. Ho, A. Jain, and P. Abbeel, "Denoising diffusion probabilistic models," *Advances in neural information processing systems*, vol. 33, pp. 6840–6851, 2020.
- [50] Y. Ye, K. Xu, Y. Huang, R. Yi, and Z. Cai, "Diffusionedge: Diffusion probabilistic model for crisp edge detection," in *Proceedings of the AAAI Conference on Artificial Intelligence*, vol. 38, no. 7, 2024, pp. 6675–6683.